A Bat-Like Sonar System for Obstacle Localization

Billur Barshan, *Student Member, IEEE,* and Roman Kuc, *Senior Member, IEEE*

Abstract—**An active wide-beam sonar system that mimics the sensor configuration of echolocating bats is described for applications in sensor-based robotics. Obstacles in a two-dimensional (2-D) environment are detected and localized using time-of-flight (TOF) measurements of their echoes. The standard threshold detector produces a biased TOF estimate. An unbiased TOF estimate is derived by a parametric fit to the echo waveform, motivated by our experimental observations of actual sonar signals. This novel method forms a trade-off between the complexity of the optimum estimator and the biased threshold detector. Using the TOF information from both methods, the range and azimuth of an obstacle are estimated. Localization is most accurate if the obstacle is located along the system line-of-sight and improves with decreasing range. Standard deviations of the range and azimuth estimators are compared to the Cramér–Rao lower bounds. The parabolic fit method has large variance but zero bias at large deviations from the line-of-sight. The system operation is generalized from isolated obstacles to extended obstacles.**

I. Introduction

ACOUSTIC SENSORS provide a convenient and inexpensive means for determining the proximity of objects, and have been useful for implementing sonar systems for robot navigation [1]–[4], registration [5], obstacle avoidance [6] and sonar map building [7], [8]. The main problem with sonar systems is that they produce measurements that require interpretation to obtain reliable results.

This paper focuses on the two-dimensional (2-D) obstacle localization problem in sensor-based robotics. Reliable obstacle localization requires complete examination of the region of interest with sonar scans [9]. Single transducer systems are limited to their angular resolution that typically equals one beam-width. For high spatial resolution, a narrow beam is desired, necessitating dense scanning of the environment to cover a particular region in space. In [10] and [11], a mobile robot, equipped with only a single rotating sonar sensor, was able to navigate from a source point to a destination through an unstructured environment. Exploiting the physical principles of the transducer and reflection processes from surfaces and edges, a navigation strategy was presented by indicating the necessary scanning pattern and the maximum step size that guarantee no collision will occur [12].

An equivalent approach is to process the data from a large number of sensors implemented as a ring array [13]. A ring of transducers brings an improvement in time, since it eliminates the need for rotations, but at the expense of an increase in the number of sensors. Possible crosstalk between the sensors must also be avoided. With either a single rotating or multiple transducer system, the slow speed of sound[1] is the fundamental limitation to completing a given robotic task in real-time. In this paper, a wide-beam sonar is employed to cover a large region in space in the time required for one pulse transmission. The signals from an array of three sensors are processed to determine the location of an obstacle. Despite the wide beam, this system still provides high-spatial resolution by exploiting the multitransducer configuration to produce an angular estimate of the object.

Our approach has been motivated by the biosonar systems of nature. Animals living in the dark are faced with the problem that vision is only of limited use. To cope with this situation, some animals have well developed auditory systems [15]. For example, most bat species are known to be capable of orientation, altitude monitoring and feeding by emitting a series of ultrasound pulses [16]. The acoustic parameters of the echoes are analyzed to obtain information on the surrounding targets such as range, angular direction and orientation, relative velocity, oscillations, target size, shape, and surface characteristics [17], [18]. Despite the relatively high attenuation of sound in air and the potential confusion of echoes from previous or subsequent pulses, those of other bats, or from other surfaces, bats do echolocate very successfully [19].

Bat echolocation was analyzed by Altes [20]–[22] who applied optimum correlation detection for binaural estimation of travel time and prey location. The problem with this technique is that it is time consuming, not only in the template matching, which may be argued is performed with minimal delay with special neural structures in the bat, but also in the observation that the correlation technique does not produce an output until the entire echo waveform is observed. We argue that bats actually do perform optimal detection, but only for distant prey for which the echo strength is small (poor signal-to-noise ratio (SNR)) and the long echo travel time allows the processing delay to be negligible. For nearby prey, on the verge of capture, time delay must be minimized to maximize bat maneuverability. In this high SNR case, the ranging must be done by faster methods that may be suboptimal, such as threshold detection, that provide a range measurement from the first time the signal exceeds a preset threshold level.

In this paper, a *bat-like* sonar system is achieved by mimicking the sensor configuration of bats and implementing some of their techniques for interpreting sonar signals. In Section II,

Manuscript received July 28, 1990; revised September 19, 1991. This work was supported by the National Science Foundation under grant ECS-8802627.

B. Barshan was with the Intelligent Sensors Laboratory, Department of Electrical Engineering, Yale University, New Haven, CT 06520, and is now with the Department of Engineering Science, University of Oxford, Oxford OX1 3PJ, UK.

R. Kuc is with the Intelligent Sensors Laboratory, Department of Electrical Engineering, Yale University, P.O. Box 2157, Yale Station, New Haven, CT 06520-2157.

IEEE Log Number 9106511.

[1]The speed of sound in air is $c = 343.5$ m/s at 20°C [14].

the sonar system is described that consists of one transmitter flanked by two receivers. The useful information is extracted directly from the initial portion of the received echo envelope rather than the high-frequency base-band signal. In Section III, a valid signal model is provided and the parameters of interest are described. Section IV investigates three methods of TOF estimation. After considering the optimal TOF estimation procedure, two suboptimal methods are developed, that are simpler to implement, much faster and adequate for obstacle localization. In Section V, estimators for object range and azimuth are derived using the TOF information. Experimental methods for verification of the analysis are presented and the results are interpreted in Section VI. Applications of the sonar system are discussed in Section VII. Standard deviations of the estimators are compared to the Cramér–Rao lower bounds derived in the Appendix.

II. Description of the Sonar System

A good sensor model provides the framework within which one can interpret sonar signal correctly. The transducer component of our sonar system, Panasonic ultrasonic ceramic microphone (EFR-OSB40K2[2]) that can be employed both for transmitting and receiving ultrasound signals is constructed using a piezoelectric ceramic with radius $a = 5.2$ mm, resonant at $f_o = 40$ kHz. In our application, it is excited by six cycles of a 30 V, 40 kHz square wave, causing an acoustic pulse to be emitted into space within a wide beam that contains the propagating pulse.

Motivated by previous experimental results [24], a valid approximation for the pressure amplitude pattern of the propagating pulse is given by

$$p(r,\theta) \cong \frac{p_o r_o}{r} e^{-\frac{\theta^2}{2\sigma_T^2}} \quad \text{for } r > r_o \tag{1}$$

where r is the radial distance from the transducer, θ is the azimuth, and p_o is the propagating pressure amplitude at range r_o along the line-of-sight ($\theta = 0°$). For our sensor, $r_o \cong 10$ cm and the beam-width parameter σ_T equals 30°. This amplitude pattern is similar to the beam of a flashlight: the cross-section forms a circular pattern that is strongest in the center and decreases with angular deviation $|\theta|$ from the center. Since the diameter of the beam cross-section increases with range, conservation of energy requires that the pressure amplitude varies inversely with range.

Equation (1) also describes, by the reciprocity principle [25], the receiving sensitivity of the transducer. The configuration for a pair of identical transducers, one acting as a transmitter T, and the other as a receiver R, is shown in Fig. 1(a). For obstacle localization in two-dimension, a vertical pole-like obstacle is convenient to work with since it is an omnidirectional reflector in the horizontal dimension. After being reflected, the cylindrical echo from a pole-like obstacle attenuates as $r^{-1/2}$ and has the following form [26]

$$A(r_1,r_2,\theta_1,\theta_2) \cong \epsilon \frac{A_o r_o^{3/2}}{r_1\sqrt{r_2}} r^{\frac{-\left(\theta_1^2+\theta_2^2\right)}{2\sigma_T^2}} \quad \text{for } r_1, r_2 > r_o \tag{2}$$

[2]Panasonic Corp. *Ultrasonic Ceramic Microphones*, 12 Blanchard Road, Burlington, MA 01803, 1989.

where r_1 and r_2 are the distances, and θ_1 and θ_2 are the angular deviations of the reflector from the transmitter and the receiver respectively. A_o is the echo amplitude observed when T and R are coincident, for which $r_1 = r_2 = r_o$ and $\theta_1 = \theta_2 = 0°$. The ϵ is the reflection coefficient of the reflector. Note that the maximum of (2) occurs at $\theta_1 = \theta_2$. In three dimensions, for a small point-like target with cross-section ϵ, the spherical echo produces the denominator term $r_1 r_2$ and (2) becomes equivalent to the well-known radar equation [27], [28].

In our bat-like sonar, the middle transducer T (mouth and/or nose or the bat) transmits an echolocation pulse, and the two receivers R1 and R2 (ears of the bat) capture the echoes reflected back by obstacles illustrated in Fig. 1(b). The *range* r and *azimuth* θ of an obstacle are measured from the transmitter, and the azimuth θ is measured with respect to the transmitter line-of-sight, taking positive values in the clockwise direction.

Two regions of sensitivity can be distinguished as shown in Fig. 2. An obstacle is detectable by *both* receivers if it lies in the *active region* of the sonar system. The active region is defined by the intersection of the echo-amplitude patterns of T-$R1$ pair and T-$R2$ pair, each given by (2). The contours shown in this figure correspond to the points where the detected amplitude is -40 dB relative to the maximum. In the *left (right) receiver region*, only $R1$ (or $R2$) can detect echoes from objects. This paper focuses on obstacle localization in the active region only.

III. Signal Observation Model

If the transmitter is excited at $t = 0$, the shape of the echo detected by the receiver, shown in Fig. 3, can be approximated by

$$y(t) = x(t - t_F)\cos[2\pi f_o(t - t_F)] + w(t) \tag{3a}$$

where $x(t - t_F)$ is the envelope of the pulse, given by

$$x(t - t_F) = a_o e^{-a_1(t-t_F)}(t - t_F)^2 u(t - t_F) \tag{3b}$$

where $u(t - t_F)$ is a unit-step function delayed by t_F, and a_o, a_1 are shape and amplitude parameters of the signal. The time-of-flight t_F corresponds to the starting point of the pulse. The signal $w(t)$ is white Gaussian noise having zero mean and variance σ_w^2. In our system, the sources of noise include *thermal noise* in the electronics, acoustic noise from the sound sources in the environment, and amplitude quantization error due to sampling the signal with a finite number of bits. The noisy echoes are processed to extract the signal envelope by rectification and lowpass filtering. After envelope detection, (3a) becomes

$$s(t) = x(t - t_F) + n(t). \tag{4}$$

The form of $x(t - t_F)$, given by (3b) and shown in Fig. 4(a), is capable of modeling observed echo envelopes for a wide variety of obstacle types located at different locations within the active region. The maximum amplitude of $x(t - t_F)$ is equal to $4a_o(a_1 e)^{-2}$ and occurs at $t = t_F + (2)/(a_1)$. This maximum value is equal to the value of $A(r_1, r_2, \theta_1, \theta_2)$ in (2).

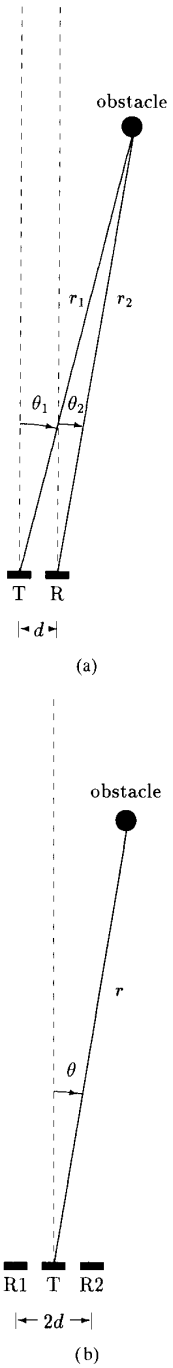

Fig. 1. (a) Pair of identical transducers, one acting as a transmitter (T), and the other as a receiver (R). (b) Sonar system configuration for obstacle localization.

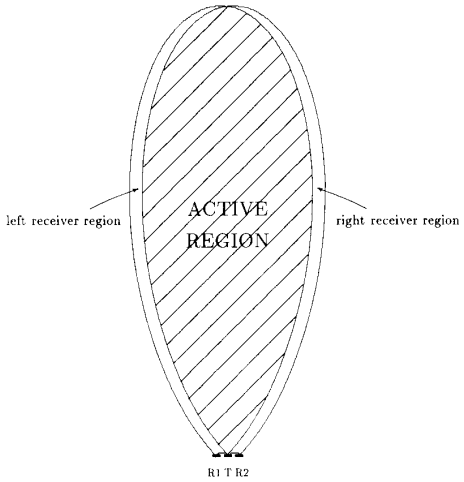

Fig. 2. Active region of the sonar system for a cylindrical reflector. For the transducer pairs T-R1 and T-R2, the equal amplitude contours of $\tilde{A}(r_1, r_2, \theta_1, \theta_2)$ corresponding to -40 dB below the maximum amplitude are drawn to scale.

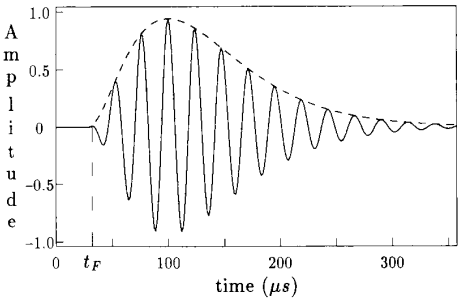

Fig. 3. Typical echo (radio frequency f_o) received from an isolated object (solid line) is simulated. Some systems determine the TOF from the envelope of the echo, shown by the dashed line. The time at which the pulse was transmitted is indicated by $t = 0$.

When there are no obstacles present in the active region, only the noise $w(t)$ is rectified and lowpass filtered. The resulting process $n(t)$ has a small mean value $\xi = \sqrt{\frac{2}{\pi}}\sigma_w$ and variance σ_n^2 determined by the amount of lowpass filtering. When the signal amplitude is significantly larger than the noise amplitude, the noise remains zero-mean after envelope detection since it is superimposed on the signal. For both cases, it can be shown by the central limit theorem [29] that $n(t)$ can be approximated by a Gaussian random process due to lowpass filtering, in which a large number of independent random variables (the thermal noise) are averaged.

The exponential term in (3b) can be neglected at the start of the envelope where $t > t_F$ and $t - t_F$ is small. A parabola is a good approximation for the onset of $x(t - t_F)$ in the time interval $[t_F, t_F + (1)/(2a_1)]$. Then, the signal observation model becomes

$$s(t) \cong a_o(t - t_F)^2 + n(t) \quad \text{for } t \in \left[t_F, t_F + \frac{1}{2a_1}\right]. \quad (5)$$

The parabolic model fit to the envelope is shown in Fig. 4(b). Uniform sampling in time produces the sequence

$$s_k \cong a_o(t_k - t_F)^2 + n_k \quad \text{for } t_k \in \left[t_F, t_F + \frac{1}{2a_1}\right] \quad (6)$$

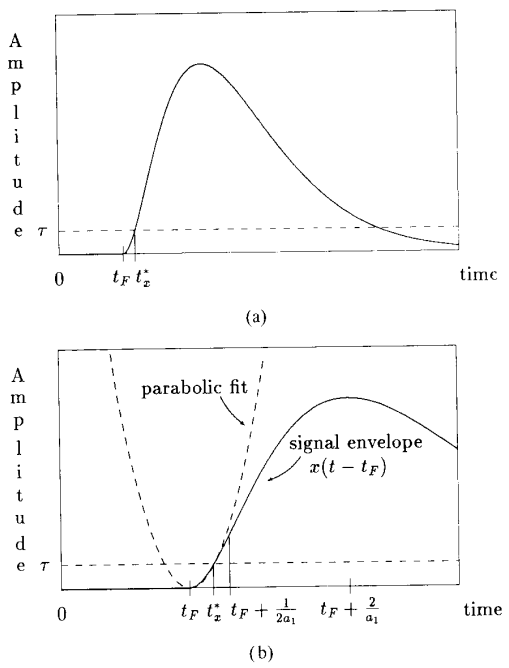

Fig. 4. (a) Envelope of typical echo received from an isolated object is simulated. The noiseless envelope exceeds the threshold τ at time t_x^*. The true value of the TOF is denoted by t_F. (b) Parabolic fit to signal envelope in the time interval $[t_F, t_F + (1)/(2a_1)]$.

where $\{t_k\}$ are the sample times, and s_k and n_k are the corresponding signal and noise samples that can be processed by a digital computer.

IV. Time-of-Flight Estimation

Analyzing the noisy echoes detected by the two receivers, the range r and azimuth θ of an obstacle in the active region of the sonar system need to be estimated from the value of TOF at each receiver. In the next section, three different methods of TOF estimation are discussed: optimal correlation detection, simple thresholding method and the parabolic fit method.

A. The Optimal Correlation Detector

The optimum method for estimating TOF from the envelope employs a matched filter that contains a replica of the echo to determine its most probable location in the observed signal [29]. This unbiased estimator maximizes the SNR. Since the echo shape varies with the location of the object within the active region, a large number of different templates are required for the correlation operation. This procedure is time-consuming, although parallel processing allows the computation time to be reduced at increased cost. There is evidence that the bat brain contains an array of parallel detectors [19], [30].

A fundamental problem with this method is the inherent time delay involved since classical correlation detection cannot be performed before the *entire echo* is observed. Hence, this method is only suitable for distant objects when the echo duration is negligible compared to the travel time. For nearby objects, it is beneficial for the estimate to be made at the beginning of the observed echo. This can be done with the simpler suboptimal methods described next.

B. Simple Thresholding Method

The method most frequently used by sonar ranging systems for extracting the TOF information is simple threshold detection [32]. A threshold level, denoted by τ, is set according to the noise level σ_n to suppress spurious readings. When the signal envelope amplitude first exceeds τ, a clock measuring the time from pulse transmission is stopped, providing the travel time. Neglecting noise, the time at which the noiseless signal envelope first crosses the threshold τ is denoted by t_x^* and shown in Fig. 4(a). Equating the noiseless $s(t)$ in (5) to τ we find

$$t_x^* \cong t_F + \sqrt{\frac{\tau}{a_o}}. \tag{7}$$

However, the time t_x, when the signal *plus noise* exceeds the threshold for the first time, need not equal t_x^*. Further, the observed TOF is also affected by the clock resolution. If the clock resolution equal the sampling interval T_s then the TOF estimate is equal to

$$\tilde{t}_F = k_F T_s = t_x + \Delta. \tag{8}$$

where Δ is a random delay due to the asynchronous nature of the echo arrival, uniformly distributed in the interval $[0, T_s)$. Since $\tilde{t}_F$ can take on values that are only discrete multiples of the clock resolution T_s, the variable Δ can be thought of as the time delay added to the continuous-valued t_x to produce the clock reading $k_F T_s$ from threshold detection.

The statistics for this estimator need to be derived to evaluate its bias and variance defined by

$$B[\tilde{t}_F] \triangleq E[\tilde{t}_F] - t_F \tag{9a}$$

$$\mathrm{Var}[\tilde{t}_F] \triangleq E[\tilde{t}_F^2] - E^2[\tilde{t}_F] \tag{9b}$$

where $E[.]$ denotes the expectation operator. Suppose that the shape parameters of the envelope, a_o and t_F are known. Given the model of the additive noise in (6), when $t_k < t_F$, s_k is a Gaussian random variable with mean ξ and variance σ_n^2. When $t_k \geq t_F$, the time-varying mean is equal to $a_o(t_k - t_F)^2$. The conditional probability density function $p(s_k|a_o, t_F)$ is given by

$$p(s_k|a_o, t_F) = \begin{cases} \frac{1}{\sqrt{2\pi}\sigma_n} \exp\left[-\frac{(s_k-\xi)^2}{2\sigma_n^2}\right] & \text{for } t_k < t_F \\ \frac{1}{\sqrt{2\pi}\sigma_n} \exp\left[-\frac{(s_k - a_o(t_k-t_F)^2)^2}{2\sigma_n^2}\right] & \text{for } t_k \geq t_F. \end{cases}$$

These are shown in Figs. 5(a) and (b). Since $\tilde{t}_F$ takes on values that are discrete multiples of T_s, the event $\{\tilde{t}_F = t_k\}$ is the noisy signal exceeding the threshold *first* at time sample t_k. The probability mass function $p_{\tilde{t}_F}(t_k)$ can be expressed as

$$p_{\tilde{t}_F}(t_k) = \mathrm{Prob}\{s_k < \tau \quad \text{for } t < t_k \quad \text{and} \quad s_k \geq \tau \quad \text{for } t = t_k\}. \tag{10}$$

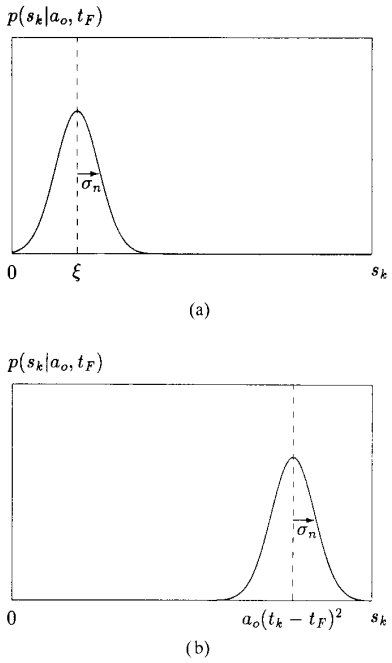

Fig. 5. (a) Probability density function of noisy signal amplitude s_k for $t_k < t_F$. (b) Probability density function of noisy signal amplitude s_k for $t_k \geq t_F$. Note that the mean $a_o(t_k - t_F)^2$ is time-varying.

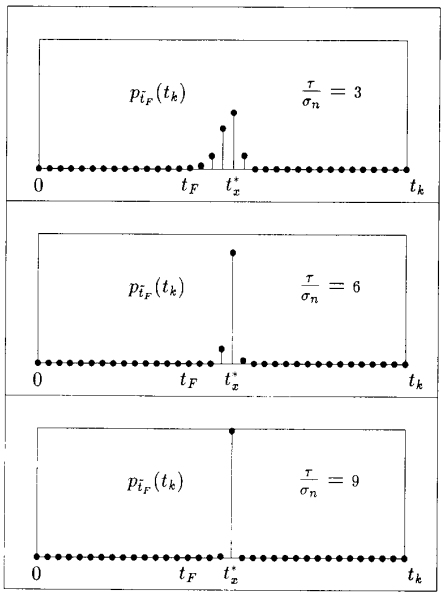

Fig. 6. Probability mass function of exceeding the threshold.

To find the probability mass function, let us assume that the samples are uncorrelated. Then

$$p_{\tilde{t}_F}(t_k) = C_o \left[\prod_{j=0}^{k-1} \int_{-\infty}^{\tau} ds_j p(s_j|a_o, t_F) \right] \left[\int_{\tau}^{\infty} ds_k p(s_k|a_o, t_F) \right]$$
$$= C_o \left[\prod_{j=0}^{k-1} \mathrm{erf}_*(x_j) \right] [1 - \mathrm{erf}_*(x_k)] \tag{11}$$

where $\mathrm{erf}_*(x_i) \triangleq \frac{1}{\sqrt{2\pi}} \int_{-\infty}^{x_i} dy \; e^{-\frac{y^2}{2}}$:

$$x_i = \begin{cases} \frac{\tau - \xi}{\sigma_n} & \text{for } t_i \leq t_F \\ \frac{\tau}{\sigma_n}\left[1 - \frac{(t_i - t_F)^2}{(t_x^* - t_F)^2}\right] & \text{for } t_i > t_F \end{cases}$$

and C_o is a normalization constant.

The mass function $p_{\tilde{t}_F}(t_k)$ evaluated for values of $\tau/\sigma_n = 3, 6, 9$ is shown in Fig. 6. As τ/σ_n increases by reducing σ_n and keeping τ constant, $p_{\tilde{t}_F}(t_k)$ approaches a Kronecker delta function located at $t_x^* + \Delta$. Therefore, for a particular obstacle, as $\sigma_n \to 0$, the mean crossover time approaches $t_x^* + \Delta$ and the variance decreases. When considering the set of all obstacles, Δ becomes a random variable that is independent of t_x^*. Taking expectations over Δ, the variance of $\tilde{t}_F$ asymptotically approaches $(T_s^2)/(12)$ as τ/σ_n increases. Since $E[\tilde{t}_F]$ approaches $t_x^* + (T_s)/2$ for high τ/σ_n, the bias is

$$B[\tilde{t}_F] = \sqrt{\frac{\tau}{a_o}} + \frac{T_s}{2}. \tag{12}$$

This illustrates the problem inherent to thresholding: for $\tau > 0$, this estimator is biased since the actual echo arrival time occurs before the time t_x where the echo exceeds the threshold. The bias varies with the location of the object in the active region, since changes in amplitude and a_o cause the threshold to be exceeded at different parts of the envelope. Where the signal amplitude is large, a_o (equal to one half the curvature of the parabola) takes larger values, yielding a smaller bias in (12). A second estimator, proposed in the next section, eliminates this bias.

C. Parabolic Fit to the Signal Envelope

As an alternative to simple thresholding, this novel estimator provides a parabolic fit to the leading edge of the echo envelope to produce the TOF estimate $\tilde{t}_F$. The parabolic fit was motivated by the empirical observations of actual sonar signals, and forms a trade-off between the complexity of the optimum correlation estimator and the biased threshold detector. One advantage of the parabolic method is that, like the thresholding method, it uses only the leading part of the echo, making it robust to temporal masking by the later-arriving echoes that tend to distort the envelope. Another advantage is that, even though the echo envelope changes as a function of obstacle location within the beam, the leading edge still retains its parabolic form, although with location-dependent parameter values.

Since the signal model (6) is *nonlinear* in $\tilde{t}_F$, an iterative algorithm proposed by Marquardt [33] is employed to estimate the values of a_o and t_F. Suppose that N samples of the signal envelope fall within the time interval $[t_F, t_F + 1/2a_1]$ where the parabolic model in (6) is valid. The algorithm starts with the initial guesses for a_o and t_F, denoted by $\hat{a}_o^{(0)}$ and $\hat{t}_F^{(0)}$, where $\hat{t}_F^{(0)}$ is set equal to $\tilde{t}_F$ from threshold detection, and $\hat{a}_o^{(0)}$ is equal to one half the derivative of the signal at $\tilde{t}_F$, obtained

TABLE I
COMPARISON OF TWO METHODS OF TOF ESTIMATION

Method	$E[t_F]$	$B[t_F]$	σ_{t_F}	$E[z]$	$B[z]$	σ_z
Thresholding	4.14 ms	62 μs	15.0 μs	1422.1 mm	21.3 mm	5.2 mm
Parabolic Fit	4.08 ms	0 μs	14.8 μs	1401.5 mm	0.0 mm	5.1 mm

True value: t_F =4.08 ms; z =1401.5 mm

by computing a discrete approximation from the time-samples. With these initial values, the squared error objective function at the nth iteration is computed:

$$\left[\mathcal{E}^2\right]^{(n)} = \sum_k \left[s_k - \hat{a}_o^{(n)}\left(t_k - \hat{t}_F^{(n)}\right)^2\right]^2 \quad \text{for } t_k \in \left[t_F, t_F + \frac{1}{2a_1}\right]. \tag{13}$$

A variable step gradient method is employed to generate trial values $\hat{a}_o^{(n)} = \hat{a}_o^{(n-1)} + \Delta\hat{a}_o^{(n-1)}$ and $\hat{t}_F^{(n)} = \hat{t}_F^{(n-1)} + \Delta\hat{t}_F^{(n-1)}$ by Marquardt's algorithm. The objective function is evaluated using these trial values. The estimate for t_F is then updated as follows:

$$\hat{t}_F^{(n)} = \begin{cases} \hat{t}_F^{(n-1)} + \Delta\hat{t}_F^{(n-1)} & \text{if } \left[\mathcal{E}^2\right]^{(n)} < \left[\mathcal{E}^2\right]^{(n-1)} \\ \hat{t}_F^{(n-1)} & \text{if } \left[\mathcal{E}^2\right]^{(n)} \geq \left[\mathcal{E}^2\right]^{(n-1)}. \end{cases} \tag{14}$$

The estimate for a_o is updated in a similar fashion. Depending on the success of the trial parameters, the step size is varied and new trial values are generated. The algorithm terminates when $\Delta\hat{t}_F^{(n-1)}$ is less than $10^{-4}T_s$, which is usually achieved within 5 to 10 iterations. Then $\hat{t}_F = \hat{t}_F^{(n)}$ and $\hat{a}_o = \hat{a}_o^{(n)}$.

With the parabolic fit method, N data points contribute information to the estimation process, whereas with simple thresholding, the TOF estimate is made as soon as the threshold is exceeded. The estimate $\hat{t}_F$ does not depend on the shape nor the steepness of the envelope as in the simple thresholding method, but only on its starting point. The accuracy is also improved because there is no random shift Δ due to sampling the envelope, since $\hat{t}_F$ need not correspond to a sample point t_k.

Since an analytic expression for $\hat{t}_F$ is not available, $E\left[\hat{t}_F\right]$ and $\mathrm{Var}\left[\hat{t}_F\right]$ cannot be determined analytically. We will determine the mean and variance by performing repeated experiments.

D. Experimental Verification of TOF Estimation

1) Methods: The block diagram of the system is shown in Fig. 7. Data acquisition is performed by the Ariel DSP-16 Signal Processing Board with two input channels having 16 bits of resolution. Echo envelopes are digitized by an A/D converter, operating at 50 kHz sampling rate per channel ($T_s = 20$ μs). The detected echo signal consists of 600 sample points yielding a total time duration of 12 ms corresponding to 2.1 m range interval. The DSP board communicates with an IBM PC/XT-286 for the processing the signals.

To compare the two suboptimal methods of estimating TOF in terms of their expected values and variances, a cylinder of diameter 16 cm and height 1 m was placed at $\theta = 0°$ and $r = 700$ mm. The transducer separation d was 60 mm. The

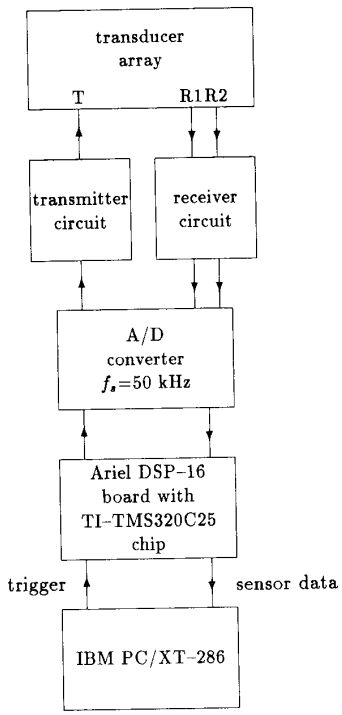

Fig. 7. Block diagram of system configuration for obstacle localization.

true TOF is $t_F = \left(r + \sqrt{r^2 + d^2}\right)/(c) = 4.08$ ms. The value for σ_n was determined by performing repeated experiments with no object present and computing the root mean square deviation of the signal amplitude. The system threshold τ was set equal to $6\sigma_n$. The amplifier gain was set so that the maximum amplitude over the active region is within the linear range the A/D converter. A pulse was transmitted and t_F was estimated by both methods of TOF estimation. One thousand trials were repeated to compute the mean values and the standard deviations.

2) Results: The results are tabulated in Table I. With the thresholding method, $E\left[\hat{t}_F\right]$ was observed to be 4.14 ms. The bias is then $B\left[\hat{t}_F\right] = 62$ μs, equivalent to 3.1 sampling intervals. In this case, the round-trip distance measurement is biased by 21.3 mm. The standard deviation of the threshold crossover point was observed to equal 15 μs, or 5.2 mm. The analytical value predicted by (3.5) is 6.0 mm, corresponding to the second case in Fig. 6. The standard deviation component $\sqrt{(T_s^2)/(12)}$ due to sampling is 5.8 μs or 2.0 mm.

With the parabolic fit method, $E\left[\hat{t}_F\right]$ was observed to be 4.08 ms, supporting the claim that the estimator is unbiased. Hence, we have an unbiased estimate of TOF having a

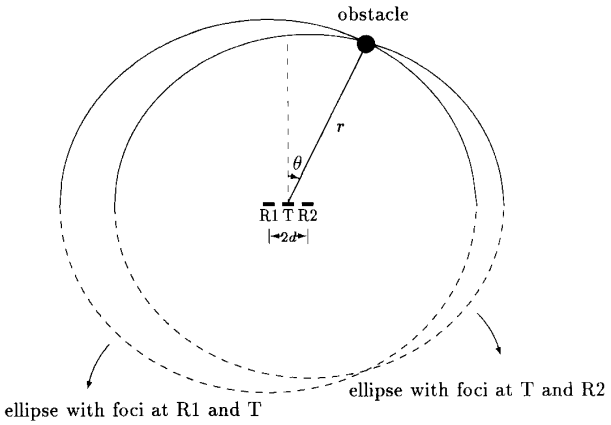

Fig. 8. Geometry of obstacle localization with a three-transducer array.

standard deviation comparable to thresholding. The trade-off of eliminating the bias is increased computation.

Having derived an unbiased estimate for t_F, we now employ it for estimating range and azimuth in the next section.

V. Range and Azimuth Estimation

When an obstacle is located at r and θ in the active region, two TOF measurements $\hat{t}_{F1}$ and $\hat{t}_{F2}$ are acquired from R1 and R2, which correspond to the round-trip distances $\hat{z}_1 = c\hat{t}_{F1}$ and $\hat{z}_2 = c\hat{t}_{F2}$ from the transmitter to each receiver. Measurement $\hat{z}_1$ restricts the possible locations for the obstacle to lie on an ellipse whose foci are at T and R1. Similarly, given $\hat{z}_2$, the possible obstacle locations lie on an ellipse with foci at T and R2, as shown in Fig. 8. Both measurements are valid only where the two ellipses intersect. Of the two intersection points, the one in the active region corresponds to the obstacle position.

From Fig. 8, the estimates of round-trip distances are given by

$$\begin{aligned} \hat{z}_1 &= \sqrt{r^2 + d^2 + 2dr\sin\theta} + r + e_1(r,\theta) \\ \hat{z}_2 &= \sqrt{r^2 + d^2 - 2dr\sin\theta} + r + e_2(r,\theta) \end{aligned} \tag{15}$$

where d is the transducer separation, $e_1(r,\theta)$ and $e_2(r,\theta)$ are the zero-mean errors associated with the distance measurements, and are equal to the error in the TOF estimate multiplied by the sonic speed c. With the following vector definition:

$$\hat{z} \triangleq \begin{bmatrix} \hat{z}_1 \\ \hat{z}_2 \end{bmatrix} \quad \boldsymbol{f}(r,\theta) \triangleq \begin{bmatrix} \sqrt{r^2 + d^2 + 2dr\sin\theta} + r \\ \sqrt{r^2 + d^2 - 2dr\sin\theta} + r \end{bmatrix}$$
$$\boldsymbol{e}(r,\theta) \triangleq \begin{bmatrix} e_1(r,\theta) \\ e_2(r,\theta) \end{bmatrix}. \tag{16}$$

Equation (16) can be written more compactly as

$$\hat{\boldsymbol{z}} = \boldsymbol{f}(r,\theta) + \boldsymbol{e}(r,\theta). \tag{17}$$

When the thermal noise dominates the acoustic noise, error components $e_1(r,\theta)$ and $e_2(r,\theta)$ can be considered uncorrelated. Therefore, $\boldsymbol{e}(r,\theta)$ is white Gaussian error with covariance matrix $\boldsymbol{C} = \sigma_e^2(r,\theta)\boldsymbol{I}$, and the conditional probability density function of $\hat{\boldsymbol{z}}$ is

$$p(\hat{\boldsymbol{z}}|r,\theta) = \frac{1}{2\pi|\boldsymbol{C}|}\exp \cdot \left\{-\frac{1}{2}[\hat{\boldsymbol{z}} - \boldsymbol{f}(r,\theta)]^T\boldsymbol{C}^{-1}[\hat{\boldsymbol{z}} - \boldsymbol{f}(r,\theta)]\right\}. \tag{18}$$

Since the maximum likelihood estimate commutes over nonlinear operations, maximum likelihood estimates [34] of r and θ are the values that maximize (18) and are given by the implicit equation:

$$\boldsymbol{f}\left(\hat{r},\hat{\theta}\right) = \hat{\boldsymbol{z}}. \tag{19}$$

Solving (19) for $\hat{r}$ and $\hat{\theta}$ yields

$$\hat{r} = \frac{\hat{z}_1^2 + \hat{z}_2^2 - 2d^2}{2(\hat{z}_1 + \hat{z}_2)} \tag{20a}$$

$$\hat{\theta} = \sin^{-1}\left[\frac{(\hat{z}_1\hat{z}_2 + d^2)(\hat{z}_1 - \hat{z}_2)}{d(\hat{z}_1^2 + \hat{z}_2^2 - 2d^2)}\right]. \tag{20b}$$

VI. Experimental Verification of Localization

A. Methods

To determine the performance characteristics, the same experimental setup and parameter values in Section IV-D-1) were used. A pulse was transmitted and by processing the two echo envelopes, TOF information was obtained. Using (20a) and b, the range and azimuth of the obstacle were estimated employing both methods of TOF estimation, $\tilde{r}$ and $\tilde{\theta}$ from $\hat{t}_{F1}$, $\hat{t}_{F2}$ and $\hat{r}$ and $\hat{\theta}$ from $\hat{t}_{F1}$, $\hat{t}_{F2}$. For a given obstacle location, the effects of noise were determined by conducting one thousand trials ($M = 1000$) and computing the means and the standard deviations of the estimators. The experiment was repeated for a collection of r and θ values within the active region of the transducer system to determine the sensitivity of the system.

B. Results and Interpretation

The results are shown in Fig. 9, where the mean value of each estimator is shown along with the three standard deviation interval, indicating 99.7% confidence for a Gaussian random variable [29].

In Fig. 9(a), the curves in dotted line correspond to the simple thresholding method, whereas the curves in dashed line to the parabolic fit method. The thresholding result indicates that $\tilde{r}$ is biased and that the bias increases with $|\theta|$. This result is expected from (12) because, for obstacles located at large $|\theta|$, the signal amplitude decreases and the echo waveform expands in time, corresponding to smaller a_o values. The parabolic fit estimator is essentially unbiased since its mean value shows small, statistically insignificant fluctuations around the true value.

In Fig. 9b, $\tilde{\theta}$ is shown to be biased because at large $|\theta|$, its mean value deviates from the true value by more three standard errors of the mean, given by $3(\sigma_{\tilde{\theta}})/(\sqrt{M})$ [35]. For example, at $\theta = 30°$, $\hat{\theta}$ equals 54.1°. The deviation from the

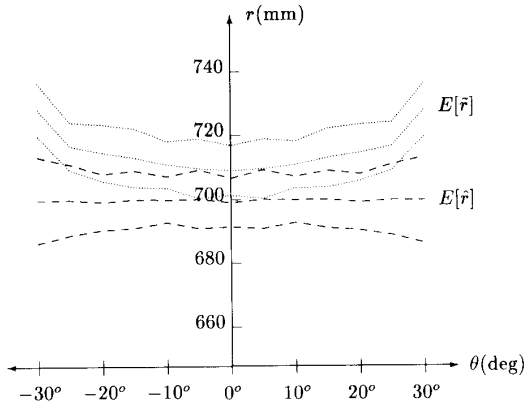

(a)

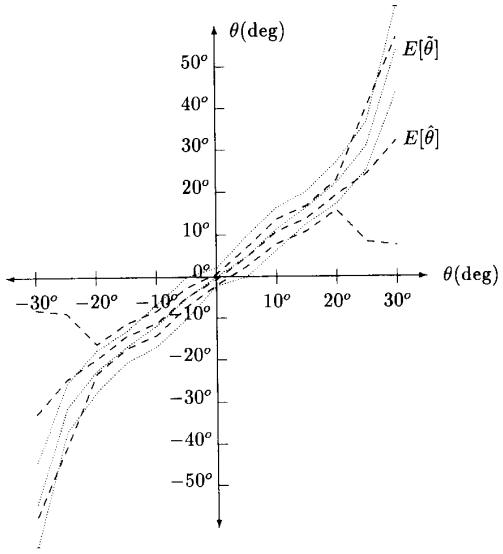

(b)

Fig. 9. (a) Comparison of the range estimators ($r = 700$ mm and $d = 60$ mm). Family of curves in dotted line shows $E[\tilde{r}] \pm 3\sigma_{\tilde{r}}$ versus θ from simple thresholding method, and the curves in dashed line correspond to $E[\hat{r}] \pm 3\sigma_{\hat{r}}$ versus θ from the parabolic fit method. (b) Comparison of the azimuth estimators ($r = 700$ mm and $d = 60$ mm). Family of curves in dotted line corresponds to the threshold detection estimator $E[\tilde{\theta}] \pm 3\sigma_{\tilde{\theta}}$ versus θ, whereas the curves in dashed line are the results $E[\hat{\theta}] \pm 3\sigma_{\hat{\theta}}$ versus θ from the parabolic fit estimator.

true value (24.1°) is much larger than $3(\sigma_{\hat{\theta}})/(\sqrt{M})$ value of 0.3°. This bias is due to the bias in TOF estimates $\tilde{t}_{F1}$ and $\tilde{t}_{F2}$.

The $\hat{\theta}$ is also slightly biased at large $|\theta|$ although less than $\tilde{\theta}$. At $\theta = 30°$, $\hat{\theta}$ equals 32.5°. The deviation from the true value is larger than the $3(\sigma_{\hat{\theta}})/(\sqrt{M})$ value of 0.8°. When TOF measurements are unbiased, $\hat{\theta}$ need not be unbiased since the azimuth estimator is a nonlinear function of t_{F1} and t_{F2} measurements.

Note that the standard deviation of each estimator is minimum at $\theta = 0°$ and increases with $|\theta|$. The standard deviation for the range estimate was also observed to increase with range. These results can be explained in terms of the echo amplitude pattern given in (1), which indicates that the echo amplitude decreases with range and with increasing deviation $|\theta|$ from the transducer line-of-sight. Since the processed echoes have smaller SNRs at larger deviations from the line-of-sight, the estimator variances are larger.

C. Comparison to Cramér–Rao Lower Bounds

To compare the performance of the estimators, Cramér–Rao lower bounds [34] for unbiased estimator variance are derived in the Appendix and evaluated as functions of range, azimuth and transducer separation. The optimum correlation detection method satisfies these lower bounds asymptotically. Although this bound is for unbiased estimators, for comparison, we have combined experimental standard deviations with the corresponding biases to compare to the lower bound. The results are shown in Figs. 10(a) and (b).

The lower bound is not achieved by the experimental results for both range estimators. However, the result from the parabolic fit method follows the lower bound very closely. Since the bias in the thresholding range estimator is significantly high, the bias-variance combination $\sqrt{\sigma_{\tilde{r}}^2 + B_{\tilde{r}}^2}$ for this estimator is approximately six times larger than the lower bound.

For $|\theta| \leq 20°$, both azimuth estimators are comparable in variance. For $|\theta| > 20°$, the parabolic fit method provides a better estimate of θ than the simple threshold detector, indicating that it is a more robust estimator when the SNR is low.

The optimum correlation detection method satisfies these lower bounds that do not consider multiple echo interference [31]. However, since the envelope of the detected signal, parametrized a_o and a_1 values, varies with range and azimuth, the optimal method requires that a large number of reference signals be stored. The simpler, suboptimal methods provide an attractive compromise between accuracy and system complexity.

VII. Discussion

A. Implication to Bat Localization

The similarity in design of our sonar system and that of the bat provides some insights on animal sonar systems. For successful capture of prey, it is crucial that the accuracy is best along the line-of-sight, which is usually the direction of flight. Furthermore, whereas high range accuracy is not necessary for remote prey, it becomes increasingly important as the range decreases to the capture point. At such close ranges where SNR is high and speed is crucial, suboptimal methods work well. This is exactly the type of behavior our system exhibits.

B. Generalization to Extended Objects

Above, we have only considered the localization of the closest isolated obstacle within the active region of the sonar system. What happens if an extended specular or rough surface occupies this region? Specular reflectors allow us to view the transmitter and the two receivers as a transmitter and two virtual receivers $R1'$ and $R2'$ as shown in Fig. 11. By tracing rays as in mirror reflectors [23], we find that the round trip distance z_1, measured by the first receiver, corresponds to the

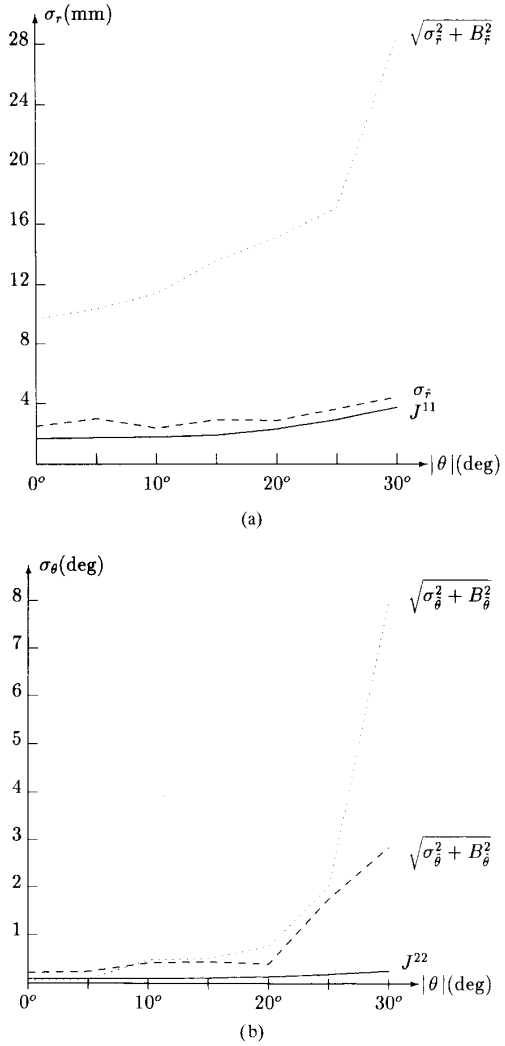

Fig. 10. (a) Comparison of the standard deviations of the range estimators to the Cramér–Rao lower bound ($r = 700$ mm and $d = 60$ mm). The lower bound is shown in solid line. The dotted line indicates $\sigma_{\tilde{r}}$ versus $|\theta|$ from simple threshold detection, and the dashed line corresponds to $\sigma_{\hat{r}}$ versus $|\theta|$ from the parabolic fit method. (b) Comparison of the standard deviations of the azimuth estimators to the Cramér–Rao lower bound ($r = 700$ mm and $d = 60$ mm). The lower bound is shown in solid line. The dotted line indicates $\sigma_{\tilde{\theta}}$ versus $|\theta|$ from simple threshold detection, and the dashed line corresponds to $\sigma_{\hat{\theta}}$ versus $|\theta|$ from the parabolic fit method.

distance between T and $R1'$. Similarly, the distance z_2 is the same as the direct path length between T and $R2'$. From the geometry, we get

$$z_1 = \sqrt{(2r + d\sin\theta)^2 + (d\cos\theta)^2} = 2r\sqrt{1 + \frac{d\sin\theta}{r} + \frac{d^2}{4r^2}} \tag{21a}$$

$$z_2 = \sqrt{(2r - d\sin\theta)^2 + (d\cos\theta)^2} = 2r\sqrt{1 - \frac{d\sin\theta}{r} + \frac{d^2}{4r^2}}. \tag{21b}$$

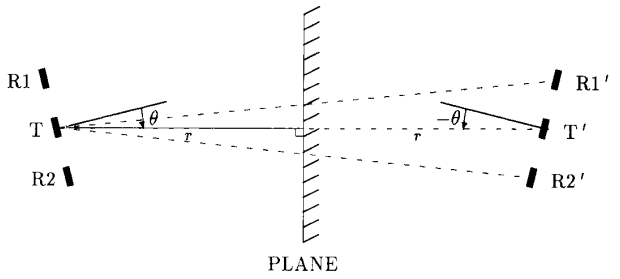

Fig. 11. Virtual transducer configuration for an extended specular reflector. Expected value of the obstacle location is at the intersection of the plane with the normal from the transmitter T.

Substituting these expressions in (20a) and (20b)

$$\hat{r} = \frac{2r}{\sqrt{1 + \frac{d\sin\theta}{r} + \frac{d^2}{4r^2}} + \sqrt{1 - \frac{d\sin\theta}{r} + \frac{d^2}{4r^2}}}. \tag{22}$$

After making a Taylor series expansion of (21a) and (21b) and neglecting the terms beyond second order since $d \ll r$:

$$\hat{r} = \frac{r}{1 - \frac{d^2\cos^2\theta}{8r^2}} \cong r \quad \text{for} \quad d \ll r. \tag{23}$$

A similar approximation for $\hat{\theta}$ yields

$$\sin\hat{\theta} = \sin\theta\sqrt{1 + \frac{d^2}{2r^2} - \frac{d^2\sin^2\theta}{r^2}} \cong \sin\theta \quad \text{for} \quad d \ll r. \tag{24}$$

Therefore, for a specular reflector, the estimates of r and θ, computed from (20a) and (20b), correspond to the location where the perpendicular path from transmitter T intersects the plane reflector. Our experiments with extended specular surfaces verify this result. For a specular reflector, the detected echo is large since the denominator in (2) becomes $r_1 + r_2$ and $\epsilon = 1$.

A very rough surface is much more complicated to analyze. As a first order approximation, it can be considered as a collection of many different targets as shown in Fig. 12. Some cancellation may occur between the baseband echoes from each target, reducing the resultant amplitude. For small thresholds, the leading edge of the resultant echo corresponds to the closest target with a favorable orientation with respect to the transducer line-of-sight [31]. This target can be anywhere within the active region of the sonar system. The intersection of the ellipses defined by the two targets may correspond to a "phantom target." Therefore, depending on orientation, $\hat{r}$ and $\hat{\theta}$ can be anywhere between the two individual targets and the phantom target in the active region. Experimentally, we observe that the expected values $E[\hat{r}]$, $E[\hat{\theta}]$ correspond to the intermediate point between the two targets.

VIII. Conclusion

A multitransducer sonar system that demonstrates a significant improvement in object localization over the standard single transducer system was described. Simple threshold

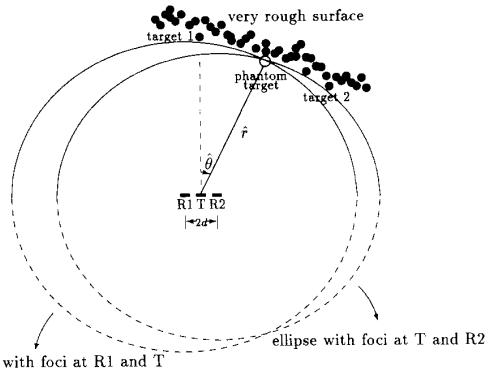

Fig. 12. Obstacle localization for a very rough surface. The phantom target at the intersection of the ellipses is shown by an empty circle. The solid dots indicate the facets of the rough surface.

detection produces a bias in the TOF measurement. An alternative parabolic fit method that eliminates the bias was described. With both methods, TOF information was extracted from the leading edge of the echo, eliminating the need for the whole pulse to be processed. This is especially important for fast response time or when there are overlapping echoes. For a measure of estimator accuracy, standard deviations of the estimates were computed as functions of range and azimuth and compared to the Cramér–Rao bounds for the optimal estimator. The operation was generalized from isolated obstacles to extended obstacles.

Appendix
Derivation of Cramér–Rao Lower Bounds

In (17), our observation model is given by

$$\hat{\boldsymbol{z}} = \boldsymbol{f}(r,\theta) + \boldsymbol{e}(r,\theta) \tag{25}$$

where $\boldsymbol{e}(r,\theta)$ is white Gaussian error with covariance matrix $\boldsymbol{C} = \sigma_e^2(r,\theta)\boldsymbol{I}$.

$$\boldsymbol{C} = \begin{bmatrix} \sigma_e^2(r,\theta) & 0 \\ 0 & \sigma_e^2(r,\theta) \end{bmatrix} \text{ and its inverse}$$
$$\boldsymbol{C}^{-1} = \begin{bmatrix} \frac{1}{\sigma_e^2(r,\theta)} & 0 \\ 0 & \frac{1}{\sigma_e^2(r,\theta)} \end{bmatrix}. \tag{26}$$

The vector $\boldsymbol{f}(r,\theta)$ is refined as

$$\boldsymbol{f}(r,\theta) = \begin{bmatrix} f_1(r,\theta) \\ f_2(r,\theta) \end{bmatrix} = \begin{bmatrix} \sqrt{r^2+d^2+2dr\sin\theta} + r \\ \sqrt{r^2+d^2-2dr\sin\theta} + r \end{bmatrix}. \tag{27}$$

For unbiased estimates of r and θ, Cramér–Rao lower bounds for estimator variances are given by the following expressions:

$$\sigma_{\hat{r}}^2 = \mathrm{var}[\hat{r}(\hat{\boldsymbol{z}}) - r] \geq J^{11} \tag{28}$$
$$\sigma_{\hat{\theta}}^2 = \mathrm{var}\left[\hat{\theta}(\hat{\boldsymbol{z}}) - \theta\right] \geq J^{22} \tag{29}$$

where J^{11} and J^{22} are the diagonal elements of the inverse of Fisher's information matrix that will be derived in this section. Equality in (28) and (29) is usually asymptotically attained for a large number of observations, i.e., the maximum likelihood estimate is asymptotically efficient [34].

Fisher's information matrix $\boldsymbol{J}$ is given by

$$\boldsymbol{J} = \begin{bmatrix} J_{11} & J_{12} \\ J_{21} & J_{22} \end{bmatrix} = \begin{bmatrix} -E\left[\frac{\partial^2 \ln p(\hat{\boldsymbol{z}}|r,\theta)}{\partial r^2}\right] & -E\left[\frac{\partial^2 \ln p(\hat{\boldsymbol{z}}|r,\theta)}{\partial r \partial \theta}\right] \\ -E\left[\frac{\partial^2 \ln p(\hat{\boldsymbol{z}}|r,\theta)}{\partial \theta \partial r}\right] & -E\left[\frac{\partial^2 \ln p(\hat{\boldsymbol{z}}|r,\theta)}{\partial \theta^2}\right] \end{bmatrix} \tag{30}$$

where $E[.]$ is the expectation operator and the probability density function $p(\hat{\boldsymbol{z}}|r,\theta)$ is given in (18). Computing the derivatives in (30), the elements of $\boldsymbol{J}$ are

$$J_{11} = \frac{\partial \boldsymbol{f}^T(r,\theta)}{\partial r}\boldsymbol{C}^{-1}\frac{\partial \boldsymbol{f}(r,\theta)}{\partial r} = \frac{A^2+B^2}{\sigma_e^2(r,\theta)} \tag{31}$$

$$J_{22} = \frac{\partial \boldsymbol{f}^T(r,\theta)}{\partial \theta}\boldsymbol{C}^{-1}\frac{\partial \boldsymbol{f}(r.\theta)}{\partial \theta} = \frac{C^2+D^2}{\sigma_e^2(r,\theta)} \tag{32}$$

$$J_{12} = J_{21} = \frac{1}{2} \cdot \left[\frac{\partial \boldsymbol{f}^T(r,\theta)}{\partial r}\boldsymbol{C}^{-1}\frac{\partial \boldsymbol{f}(r,\theta)}{\partial \theta} + \frac{\partial \boldsymbol{f}^T(r,\theta)}{\partial r}\boldsymbol{C}^{-1}\frac{\partial \boldsymbol{f}(r,\theta)}{\partial r}\right] = \frac{AC+BD}{2\sigma_e^2(r,\theta)} \tag{33}$$

where

$$A = \frac{\partial f_1(r,\theta)}{\partial r} = \frac{r + d\sin\theta}{\sqrt{r^2+d^2+2dr\sin\theta}} + 1 \tag{34}$$

$$B = \frac{\partial f_2(r,\theta)}{\partial r} = \frac{r - d\sin\theta}{\sqrt{r^2+d^2-2dr\sin\theta}} + 1 \tag{35}$$

$$C = \frac{\partial f_1(r,\theta)}{\partial \theta} = \frac{dr\cos\theta}{\sqrt{r^2+d^2+2dr\sin\theta}} \tag{36}$$

$$D = \frac{\partial f_2(r,\theta)}{\partial \theta} = \frac{-dr\cos\theta}{\sqrt{r^2+d^2-2dr\sin\theta}}. \tag{37}$$

The previous expressions are evaluated at the true values of r and θ. Expressing the information matrix in terms of A, B, C and D:

$$\boldsymbol{J} = \frac{1}{2\sigma_e^2(r,\theta)}\begin{bmatrix} 2(A^2+B^2) & AC+BD \\ AC+BD & 2(C^2+D^2) \end{bmatrix}. \tag{38}$$

Inverting $\boldsymbol{J}$, we get the matrix $\boldsymbol{J}^{-1}$ whose diagonal elements provide the lower bounds for the variances

$$\boldsymbol{J}^{-1} = \begin{bmatrix} J^{11} & J^{12} \\ J^{21} & J^{22} \end{bmatrix} \tag{39}$$

$$= \frac{2\sigma_e^2(r,\theta)}{3(A^2C^2+B^2D^2)+4(A^2D^2+B^2C^2)-2ABCD} \cdot \begin{bmatrix} 2(C^2+D^2) & -(AC+BD) \\ -(AC+BD) & 2(A^2+B^2) \end{bmatrix}. \tag{40}$$

Substituting the expressions for A, B, C and D:

$$J^{11} = \frac{4(C^2 + D^2)\sigma_e^2(r,\theta)}{3(A^2C^2 + B^2D^2) + 4(A^2D^2 + B^2C^2) - 2ABCD} \tag{41}$$

$$J^{22} = \frac{4(A^2 + B^2)\sigma_e^2(r,\theta)}{3(A^2C^2 + B^2D^2) + 4(A^2D^2 + B^2C^2) - 2ABCD}. \tag{42}$$

Note that the lower bounds J^{11} and J^{22} are functions of r, θ, and d, and are proportional to the error variance $\sigma_e^2(r,\theta)$ associated with the round-trip distance measurement. The values of $\sigma_e^2(r,\theta)$ for different range and azimuth values have been experimentally determined and used for evaluating these bounds.

REFERENCES

[1] J. L. Crowley, "Navigation for an intelligent mobile robot," *IEEE Trans. Robotics Automat.*, vol. RA-1, pp. 31–41, Mar. 1985.

[2] H. F. Durrant-Whyte and J. J. Leonard, "Navigation by correlating geometric sensor data," in *Proc. IEEE/RSJ Int. Workshop on Intelligent Robots Syst.*, Tsukuba, Japan, Sept. 4–6, 1989, pp. 440–447.

[3] A. M. Flynn, "Combining sonar and infrared sensors for mobile robot navigation," *Int. J. Robotics Res.*, vol. 7, pp. 5–14, Dec. 1988.

[4] D. J. Kriegman, E. Triendl, and T. O. Binford, "A mobile robot: sensing, planning and locomotion," in *Proc. IEEE Int. Conf. Robotics Automat.*, pp. 402–408, Raleigh, NC, Mar. 31–Apr. 3, 1987.

[5] M. Drumheller, "Mobile robot localization using sonar," *IEEE Trans. Pattern Anal. Machine Intell.*, vol. PAMI-9, pp. 325–332, March 1987.

[6] J. Borenstein and Y. Koren, "The vector field histogram: Fast obstacle avoidance for mobile robots," *IEEE Trans. Robotics Automat.*, vol. 7, pp. 278–288, June 1991.

[7] A. Elfes, "Sonar based real-world mapping and navigation," *IEEE Trans. Robotics Automat.*, vol. RA-3, pp. 249–265, June 1987.

[8] Ö. Bozma and R. Kuc, "Building a sonar map in a specular environment using a single mobile transducer," *IEEE Trans. Pattern Anal. Machine Intell.*, vol. 13, pp. 1260–1269, 1991.

[9] H. P. Moravec and A. Elfes, "High resolution maps from wide angle sonar," in *Proc. IEEE Int. Conf. Robotics Automat.*, San Francisco, CA, Apr. 7–10, 1986, pp. 116–121.

[10] R. Kuc and B. Barshan, "Navigating vehicles through an unstructured environment with sonar," in *Proc. IEEE Int. Conf. Robotics Automat.*, Scottsdale, AZ, May 14–19, 1989, pp. 1422–1427.

[11] R. Kuc and B. V. Viard, "A physically-based navigation strategy for sonar-guided vehicles," *Int. J. Robotics Res.*, vol. 10, pp. 75–87, Apr. 1991.

[12] R. Kuc, "A spatial sampling criterion for sonar obstacle detection," *IEEE Trans. Pattern Anal. Machine Intell.*, vol. 12, pp. 686–690, July 1990.

[13] S. A. Walter, "The sonar ring: obstacle detection for a mobile robot," in *Proc. IEEE Int. Conf. Robotics Automat.*, Raleigh, NC, Mar. 31–Apr. 3, 1987, pp. 1574–1578.

[14] R. C. Weast, *CRC Handbook of Chemistry and Physics.* Cleveland, OH: Chemical Rubber Co., 59th ed., 1979.

[15] A. Novick, "Acoustic orientation," in *Biology of Bats*, W. A. Wimsatt, Ed. New York: Academic, 1977, ch. 2, pp. 74–273.

[16] W. M. Masters, S. C. Jacobs and J. A. Simmons, "The structure of echolocation sounds used by the big brown bat *Eptesicus Fuscus:* some consequences for echo processing," *J. Acoust. Soc. Amer.*, vol. 89, pp. 1402–1413, Mar. 1991.

[17] R. G. Busnel and J. F. Fish, Ed., *Animal Sonar Systems.* New York: Plenum, 1980. (*Proc. Second Int. Interdisciplinary Symp. Animal Sonar Syst.*, Jersey, Channel Islands, Apr. 1–8, 1979, sponsored by NATO Advanced Study Institute.)

[18] M. J. Novacek, "Navigators of the night," *Natural History*, vol. 97, pp. 67–71, Oct. 1988.

[19] N. Suga, "Biosonar and neural computation in bats," *Scientific Amer.*, vol. 262, pp. 60–68, June 1990.

[20] R. A. Altes, "Angle estimation and binaural processing in animal echolocation," *J. Acoust. Soc. Amer.*, vol. 63, pp. 155–173, Jan. 1978.

[21] R. A. Altes, "Detection and classification phenomena of biological systems," in *Adaptive Methods in Underwater Acoustics*, H. G. Urban, Ed. New York: D. Reidel, 1985, pp. 537–554.

[22] R. A. Altes, "Bioacoustic systems: insights for acoustical imaging and pattern recognition," in *Proc. SPIE International Symp. Pattern Recog. Acoust. Imaging*, L. A. Ferrari, Ed., 1987, pp. 61–68.

[23] R. Kuc and M. W. Siegel, "Physically-based simulation model for acoustic sensor robot navigation," *IEEE Trans. Pattern Anal. Machine Intell.*, vol. PAMI-9, pp. 766–778, Nov. 1987.

[24] B. Barshan and R. Kuc, "Differentiating sonar reflections from corners and planes by employing an intelligent sensor," *IEEE Trans. Pattern Anal. Machine Intell.*, vol. 12, pp. 560–569, June 1990.

[25] M. S. Smith, *Introduction to Antennas.* New York: Springer-Verlag, 1988.

[26] P. M. Morse and K. U. Ingard, *Theoretical Acoustics.* New York: McGraw-Hill, 1968.

[27] N. S. Tzannes, *Communication and Radar Systems*, pp. 111–113. Englewood Cliffs, NJ: Prentice-Hall, 1985.

[28] A. L. Maffett, Ed., *Topics for a Statistical Description of Radar Cross Section.* New York: Wiley, 1989.

[29] A. Papoulis, *Probability, Random Variables and Stochastic Processes*, second ed. New York: McGraw-Hill, 1984.

[30] N. Suga, "Cortical computational maps for auditory imaging," *Neural Networks*, vol. 3, no. 1, pp. 3–21, 1990.

[31] A. Zeira and P. M. Schultheiss, "Time delay estimation for closely spaced echoes," in *Proc. IEEE Int. Conf. Acoust., Speech Signal Processing*, pp. 2763–2766, Albuquerque, NM, Apr. 3–6, 1990.

[32] C. Biber, S. Ellin, E. Sheck and J. Stempeck, "The Polaroid ultrasonic ranging system," in *Proc. 67th Audio Engineering Soc. Convention*, 1990. (Reprinted in Polaroid Ultrasonic Ranging System Handbook).

[33] D. W. Marquardt, "An algorithm for least squares estimation of nonlinear parameters," *SIAM J.*, vol. 11, pp. 431–441, 1963.

[34] H. L. Van Trees, *Detection, Estimation, and Modulation Theory, Part I.* New York: Wiley, 1968.

[35] M. Schwartz and L. Shaw, *Signal, Processing: Discrete Spectral Analysis, Detection, and Estimation.* New York: McGraw-Hill, 1975.

Billur Barshan (S'89) was born in Istanbul, Turkey, in 1964. She received the B.S.E.E. degree and the B.S. degree in physics from Boğaziçi University, Istanbul, Turkey, in 1986, and the M.S. and Ph.D. degrees in electrical engineering from Yale University, New Haven, CT, in 1988 and 1991, respectively.

Recently, she joined the Robotics Research Group at University of Oxford, Oxford, UK, as a postdoctoral research associate. Her current research interests include sensor-based robotics, sensor fusion and biosonar.

Roman Kuc (M'77–SM'89) received the B.S.E.E. degree from the Illinois Institute of Technology, Chicago, IL, and the Ph.D. degree in electrical engineering from Columbia University, New York, NY.

From 1968 to 1975 he was a member of technical staff at Bell Laboratories, engaged in the design of audio instrumentation and in the development of efficient speech coding techniques. From 1977 to 1979, he was a postdoctoral research associate in the Department of Electrical Engineering, Columbia University, and the Radiology Department, St. Luke's Hospital, where he applied digital processing to extract information from diagnostic ultrasound signals. In 1979, he joined the Department of Electrical Engineering, Yale University, New Haven, CT, where as the Director of the Intelligent Sensors Laboratory he is pursuing research in the solution of inverse problems and in intelligent sensors for robotics and biomedical applications. He is the author of *Introduction to Digital Signal Processing.*

Dr. Kuc is a past chairman of the Instrumentation Section of the New York Academy of Sciences and member of the board of advisers of the Medical College in Lviv, Ukraine.